NANO LETTERS

pubs.acs.org/NanoLett
Letter

Metasurface of Strongly Coupled Excitons and Nanoplasmonic Arrays

Farsane Tabataba-Vakili,*,⊥ Lukas Krelle,⊥ Lukas Husel, Huy P. G. Nguyen, Zhijie Li, Ismail Bilgin, Kenji Watanabe, Takashi Taniguchi, and Alexander Högele*

Cite This: *Nano Lett.* 2024, 24, 10090−10097

ABSTRACT: Metasurfaces allow light to be manipulated at the nanoscale. Integrating metasurfaces with transition metal dichalcogenide monolayers provides additional functionality to ultrathin optics, including tunable optical properties with enhanced light−matter interactions. In this work, we demonstrate the realization of a polaritonic metasurface utilizing the sizable light−matter coupling of excitons in monolayer WSe_2 and the collective lattice resonances of nanoplasmonic gold arrays. We developed a novel fabrication method to integrate gold nanodisk arrays in hexagonal boron nitride and thus simultaneously ensure spectrally narrow exciton transitions and their immediate proximity to the near-field of array surface lattice resonances. In the regime of strong light−matter coupling, the resulting van der Waals metasurface exhibits all key characteristics of lattice polaritons, with a directional and linearly polarized far-field emission profile dictated by the underlying nanoplasmonic lattice. Our work can be straightforwardly adapted to other lattice geometries, establishing structured van der Waals metasurfaces as means to engineer polaritonic lattices.

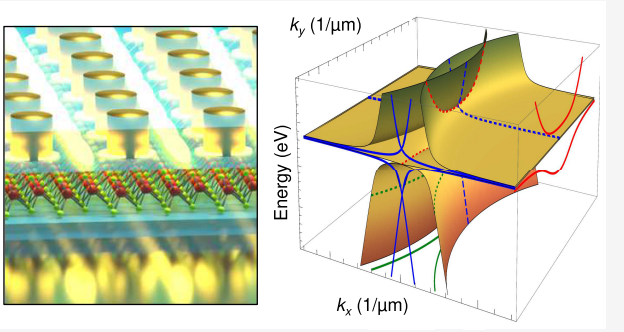

KEYWORDS: *two-dimensional semiconductors, plasmonic surface lattice resonance, metasurface, strong-coupling, exciton-plasmon-polaritons, nanoplasmonic array*

Ultrathin optical components known as metasurfaces have the potential to strongly impact modern optics by offering new functionality and unprecedented compactness. Comprised of periodic arrays of subwavelength nanostructures, metasurfaces modulate the amplitude, phase, or polarization of incident light.[1−3] Plasmonic metasurfaces consisting of metallic nanostructures provide strong field enhancement and have been used to introduce abrupt phase changes,[4] create holograms,[5] and realize ultrathin lenses.[6] While the localized surface plasmon resonances of individual nanoparticles suffer from dephasing and dissipative losses, periodic arrays of such nanoparticles with lattice constants in the order of the wavelength allow to couple the plasmon resonance to the diffractive orders of the lattice, giving rise to collective surface lattice resonances (SLRs) with quality factors exceeding 2000 at telecom wavelengths[7] and geometry-specific, angle-dependent dispersions.[8,9]

Van der Waals semiconductors are ideal building blocks for adding new functionality to metasurfaces due to their rich optical properties,[10] intrinsic two-dimensionality and ease of integration by viscoelastic stamping.[11] Monolayers of transition metal dichalcogenides (TMDs) are particularly appealing due to direct bandgaps,[12,13] large exciton binding energies,[14,15] high oscillator strengths,[16,17] and valley-selective chiral optical transitions,[18−20] with recent demonstrations of resonance tuning of atomically thin lenses,[21] separation of valley excitons,[22] and strong light−matter coupling with dielectric[23−25] and plasmonic cavities.[26−28] However, integrating TMDs with plasmonic nanostructures without compromising the optical quality of pristine TMD monolayers is challenging, as they exhibit a strong sensitivity to strain[29] and dielectric disorder[30] due to their two-dimensional nature.

The prime strategy for reducing the detrimental effects of strain and environmental disorder on the optical properties of TMD monolayers is provided by encapsulation between layers of hexagonal boron nitride (hBN) that ensure an atomically flat and clean dielectric environment.[31] However, an hBN spacer between the TMD and the plasmonic nanoparticles would prevent immediate proximity to the near-field and thus reduce the coupling strength significantly. To date, this caveat has not been resolved in coupled exciton-plasmon systems,

Received: April 29, 2024
Revised: July 16, 2024
Accepted: July 17, 2024
Published: August 6, 2024

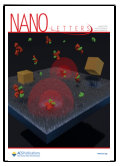

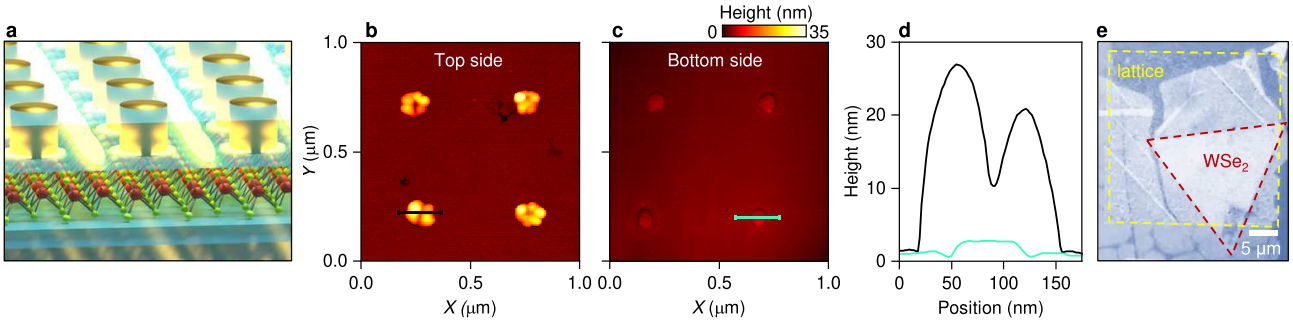

Figure 1. Plasmon−exciton−polariton van der Waals metasurface. a, Illustration of the metasurface and the near-field of the plasmonic surface lattice resonance. The sample consists of a TMD monolayer sandwiched between two hBN flakes, with a gold nanodisk lattice embedded in the top hBN layer. **b** and **c**, Atomic force micrographs of the top and bottom sides of a gold nanodisk array imprinted in hBN. The bottom side was measured with the hBN lattice flake on a PDMS/PCL stamp. **d**, Height profiles of individual gold nanodisks indicated by the black and green lines in **b** and **c**. **e**, False-color optical micrograph of the sample, with dashed lines indicating the lattice and the WSe_2 monolayer.

realizing either direct contact between plasmonic nanostructures and TMD monolayers void of hBN encapsulation[26−28,32−35] and thus subject to compromised optical quality, or using hBN-encapsulated monolayers on plasmonic nanostructures[36−38] without immediate access to the near-field.

In this work, we demonstrate strong coupling in a TMD-based plasmon-exciton-polariton metasurface utilizing a novel fabrication method. The approach we developed allows to integrate a gold nanodisk array directly into an hBN layer, and thus realize a van der Waals metasurface with immediate proximity between the near-field of the nanoplasmonic array and the TMD monolayer preserving the benefits of hBN-encapsulation. Both aspects of the integrated system ensure strong coupling between the TMD monolayer exciton and the SLR of the plasmonic nanodisc array, giving rise to plasmon-exciton-polaritons with large Rabi splitting and effective polariton dispersion conditioned by the geometry of the plamonic lattice. Consistently, the resulting emission profile of the lower polariton branch is strongly modified as compared to the emission characteristics of uncoupled monolayer excitons, exhibiting narrow-angle directional light emission with high degree of linear polarization, as dictated by the SLRs of a square lattice.

Our van der Waals metasurface, illustrated in Figure 1a, contains a WSe_2 monolayer synthesized by chemical vapor deposition[39] and high quality hBN-layers on both sides. In the top hBN layer, we incorporated a plasmonic gold nanodisk array by dry-etching through-holes into hBN and filling them with gold (details in the Methods). Atomic force micrographs of the top and bottom sides of the hBN layer with the imprinted gold lattice are shown in Figure 1b and c, and the linecuts of the respective height profiles in Figure 1d. Clearly, the bottom side with a change in height of around 1.5 nm (while suspended on the stamp) is significantly smoother than the top side, where individual gold disks reach out above the hBN-surface by as much as ∼25 nm. An additional key advantage of the bottom surface for further integration with the TMD monolayer is the fact that it was not directly exposed to any processing. Placing the bottom side on top of the TMD monolayer thus results in a flat and clean interface with immediate proximity to the near-field of the plasmonic SLRs. Moreover, the robustness of the lattice and adherent TMD allows consecutive pickup of the coupled system from the substrate via the hot-pickup technique,[11] as confirmed by the optical micrograph of the van der Waals heterostructure shown in Figure 1e. Subsequently, the stack was deposited on the terminating bottom hBN-layer on a glass substrate.

First, we determined the dispersion of the bare gold lattice in hBN using differential reflectance (DR) spectroscopy with data in Figure 2a and b. The geometric model of the diffractive orders of the SLRs,[9] illustrated in Figure 2f for momentum along the k_y axis, identifies the four lowest diffractive orders $(\pm1, 0)$ and $(0, \pm1)$ of the SLRs. For the square lattice, linearly polarized excitations couple either to the $(\pm1, 0)$ or $(0, \pm1)$ diffractive orders, which show degenerate hyperbolic (Figure 2a) or nondegenerate linear (Figure 2b) energy dispersions depending on the combination of linear polarization and k-space detection axes. With the k-vector of the SLRs given by $k_{SLR} = k_{DO} + k_{||}$, the energy dispersion is given by[9]

$$E_{SLR}(k_x, k_y) = \frac{\hbar c}{n_{eff}} \sqrt{\left(\frac{2n\pi}{a} + k_x\right)^2 + \left(\frac{2m\pi}{a} + k_y\right)^2} \quad (1)$$

with the lattice constant a, diffractive orders (n, m), and effective refractive index n_{eff}. In the long-wavelength limit at $k = 0$, $\lambda_{SLR} \approx n_{eff}a$. By fitting eq 1 to the dispersions measured at different positions on the uncoupled lattice and averaging over an area of ∼400 μm^2, we determined $n_{eff} = 1.517 \pm 0.007$ and $E_{SLR} = 1.70 \pm 0.01$ eV at $k = 0$. The best-fit procedure also yields the half-width at half-maximum linewidth of the inhomogeneously broadened Gaussian SLR in phase-corrected DR (obtained using the Kramers−Kronig relation) as $\gamma_{SLR} = 27$ meV, much narrower than for localized surface plasmons at the same energy[38] and corresponding to a quality factor of 32.

In sample regions of the van der Waals metasurface, strong coupling between the plasmonic SLRs and the bright monolayer exciton X gives rise to exciton-polaritons, with the energy dispersion of the upper (E_{UP}) and lower (E_{LP}) polariton branches given by (see the Methods for details)

$$E_{UP,LP}(k_x, k_y) = \frac{E_{SLR} + E_X - i(\gamma_X - \gamma_{SLR})}{2} \pm \sqrt{g^2 - \frac{1}{4}[E_X - E_{SLR} - i(\gamma_X - \gamma_{SLR})]^2} \quad (2)$$

where E_X and γ_X are the exciton energy and half-width at half-maximum linewidth, respectively, and g denotes the light−matter coupling strength. Representative experimental dispersions of the coupled system, recorded in DR spectroscopy, are shown in Figure 2c and d.

https://doi.org/10.1021/acs.nanolett.4c02043
Nano Lett. 2024, 24, 10090−10097

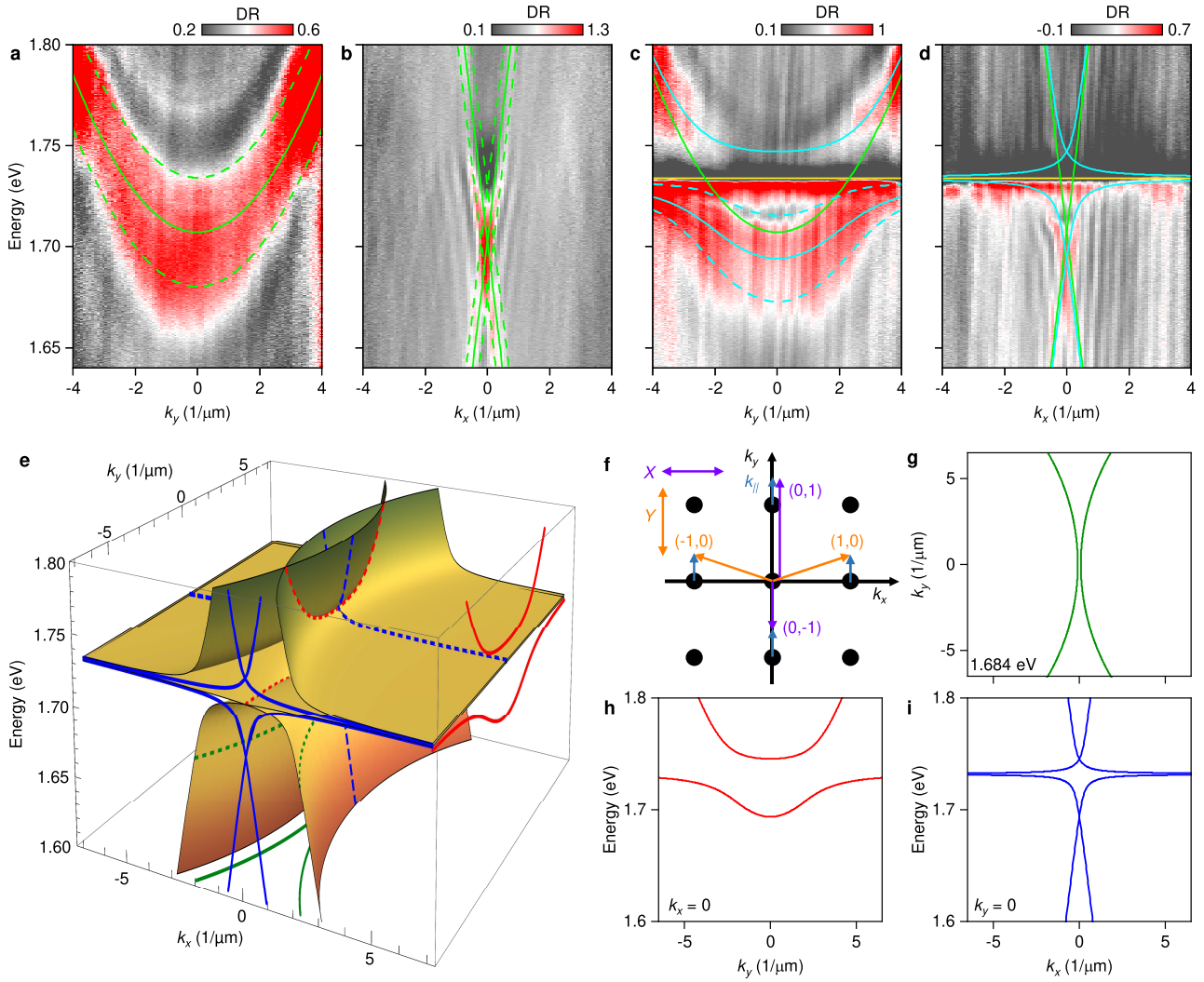

Figure 2. Momentum-resolved lattice and polariton dispersions. **a** and **b**, Hyperbolic and linear dispersions of the (±1, 0) SLRs of the uncoupled lattice in differential reflectance (DR) with linear excitation along Y and detection along k_y and k_x, respectively. Solid (dashed) lines indicate the fitted dispersions (linewidth of γ_{SLR} = 27 meV). **c** and **d**, DR polariton dispersions with linear excitation along Y and detection along k_y and k_x, respectively. The SLRs (green), bare exciton energy (yellow), and fitted polariton branches (cyan) are overlaid. Dashed cyan lines in **c** indicate the lower polariton linewidth γ_{LP}. The light−matter coupling strength g was determined as 25 meV from the best fit. **e**, Three-dimensional plot of the plasmon-exciton-polariton energy dispersion of the Y-polarized SLR branches with (±1, 0) diffractive orders, according to eq 2. **f**, Reciprocal lattice of a square lattice with in-plane k-vector $k_{||}$ along k_y. The four lowest diffractive orders (±1, 0) and (0, ±1) as well as linear polarization along X and Y are indicated. **g**−**i**, Two-dimensional projections of the dispersion in **e** for E = 1.684 eV (**g**), k_x = 0 (**h**), and k_y = 0 (**i**), with panels **h** and **i** corresponding to **c** and **d**, respectively.

By fitting eq 2 to the polariton dispersions recorded on different positions and averaging over an area of ∼300 μm^2 of the metasurface, with the exciton linewidth γ_X = 3.5 meV determined from Lorentzian fits to the phase-corrected DR on a monolayer region, we found g = 25 ± 2 meV for the light−matter coupling strength, n_{eff} = 1.513 ± 0.005 for the effective refractive index, and E_X = 1.731 ± 0.003 eV for the exciton energy in the metasurface region. The corresponding three-dimensional plot of the upper and lower polariton branches formed by the Y-polarized (±1, 0) diffractive orders is shown in Figure 2e for the square lattice geometry defined in Figure 2f, and the respective two-dimensional projections in Figure 2g−i. The fitting procedure yields a Rabi splitting Ω of 44 ± 5 meV (see the Methods for details) for the strongly coupled light−matter system, much larger than previously reported for polaritons in a TMD monolayer coupled to a dielectric metasurface.[25] Given the numbers for the competing coherent and incoherent processes, our polaritonic system clearly fulfills the common criteria for strong coupling, $g > |\gamma_X - \gamma_{SLR}|/2$ and $\Omega > \gamma_X + \gamma_{SLR}$.[40,41]

With this quantitative understanding of the polaritonic van der Waals metasurface, we inspect its emission characteristics with momentum-resolved photoluminescence (PL) spectroscopy. The respective data in Figure 3a include contributions from both the strongly coupled monolayer excitons forming lattice polaritons and their uncoupled counterparts. To begin with the latter, we first note that the spectrum of the bare WSe_2 monolayer is known to be rich: in addition to the fundamental exciton X which strongly couples to SLRs to form the upper and lower polariton branches, we observe the PL of the biexciton XX[42−45] and the spin-forbidden dark exciton D,[46,47] red-shifted from X by 19 and 43 meV, respectively. Additional contributions to zero-momentum dipolar PL include the negative trion doublet X_1^- and X_2^- with 6 meV exchange

https://doi.org/10.1021/acs.nanolett.4c02043
Nano Lett. 2024, 24, 10090−10097

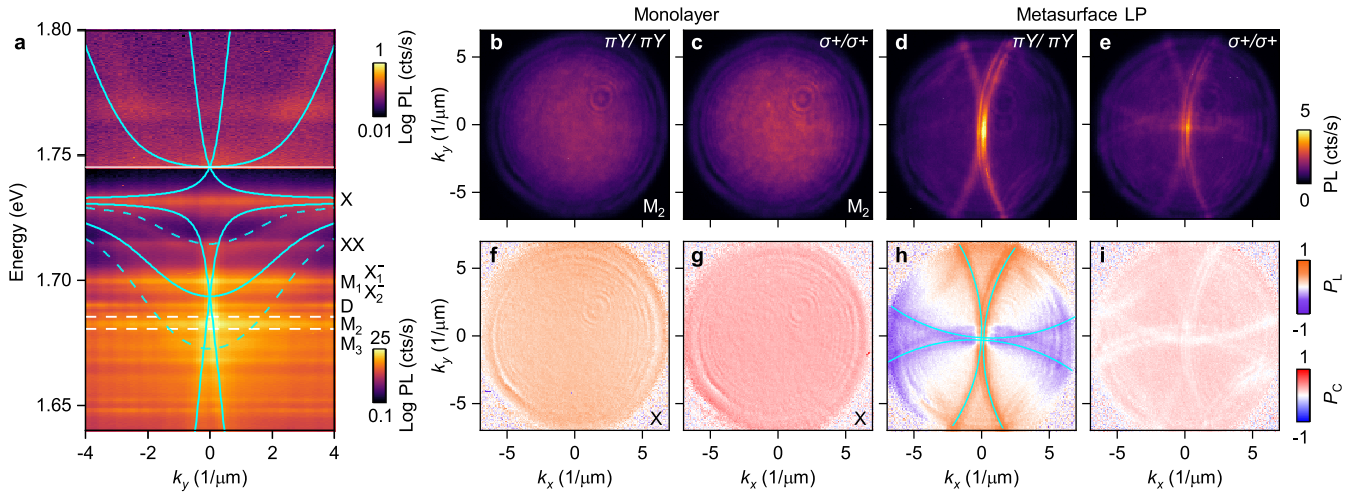

Figure 3. Momentum-resolved photoluminescence. **a**, Momentum-dispersed PL from the metasurface region, recorded with laser excitation at 1.87 eV along *Y*, shown together with the hyperbolic and linear dispersions of the upper and lower polariton branches $E_{LP,UP}$ (solid cyan lines) and the inhomogeneous broadening γ_{LP} of the hyperbolic lower polariton (dashed cyan lines). Note the different intensity scales in the top and bottom parts for better visualization of the upper polariton branch PL. **b** and **c**, Momentum-space PL images of the phonon sideband M_2 on a bare WSe_2 monolayer with Gaussian emission profile in both linear and circular polarization bases. The excitation was linear along *Y* (πY) or circular ($\sigma+$) and the detection was co-polarized, as indicated in each panel. **d** and **e**, Same but for the metasurface in the energy range delimited by white dashed lines in **a**. **f** and **g**, Degrees of linear and circular polarization, P_L and P_C, of the bright exciton X in monolayer WSe_2. **h** and **i**, Same but for the lower polariton branch of the metasurface, with dispersions of the four lowest diffractive orders shown by solid lines in **h**.

splitting,[48] visible in our sample on both bare and coupled monolayers without corresponding signatures in differential reflectance, which is consistent with low residual doping. Finally, momentum-indirect excitons contribute with a series of PL sideband peaks labeled as M_1 through M_3. The assignment of M_1 at 33 meV red-shift remains ambiguous, with direct PL emission from momentum-indirect KK'[49−51] or a phonon sideband of KQ excitons[52] as possible origins. The peaks M_2 and M_3 at 50 and 59 meV red-shifts are consistently attributed to phonon sidebands of momentum-indirect KK' excitons.[49,50]

To place emphasis on the emission characteristics of the polaritonic metasurface, we select an energy range of 4 meV centered at 1.683 eV. This energy range, slightly below the lower polariton maximum intensity, is void of any dipole-active transition of the bare monolayer. Note that even though M_2 is included in this spectral window, it has no means of coupling to the SLRs due to its momentum-indirect origin as phonon sideband with vanishingly small oscillator strength. Therefore, it contributes to the momentum-resolved PL characteristics its monolayer-specific background of out-of-plane dipolar emission, shown in Figure 3b and c. The structured emission profiles in Figure 3d and e, in contrast, are dominated by the characteristics of the metasurface lower polariton, exhibiting strong momentum narrowing and sensitivity to linear polarization. Under linear excitation and co-polarized detection, we observe a linearly polarized, directional far-field emission profile (Figure 3d), with a large fraction of the emission constrained to small angles of up to 12° at maximum k_y. Under circularly polarized excitation and detection, both sets of linearly polarized branches with orthogonal orientation are observed simultaneously (Figure 3e).

Clearly, the directional narrow-angle emission of the metasurface lower polariton is imprinted by the SLRs of the underlying nanoplasmonic square lattice (cf. Figure 2g). It also dictates the polarization characteristics of the coupled system, that is strongly modified as compared to the bare monolayer exciton transition. This effect is highlighted best by the direct comparison of the respective degrees of linear and circular PL polarization P_L and P_C, determined from polarization-resolved PL as $P_{L/C} = (I_{co} - I_{cross})/(I_{co} + I_{cross})$, where $I_{co/cross}$ are the co/cross-polarized PL intensities. The monolayer WSe_2 exciton X is known to exhibit high degrees of valley coherence and polarization,[19,53−55] quantified by the respective degrees of linear and circular polarization of dipole-characteristic emission profile in Figure 3f and g. As the emission of the lower polariton branch is not dipolar but dictated by the underlying lattice, its degree of linear polarization in Figure 3h is highly structured in momentum space (reaching values of up to 60%), as anticipated from the dispersions of the four lowest diffractive orders shown by the solid lines. The same dispersions are also evident in Figure 3i as lines of vanishing degree of circular polarization on a weak background of finite P_C stemming from M_2 PL within the spectral window of integration.

In conclusion, our work establishes lattices of exciton-polaritons by strong coupling of the fundamental TMD monolayer exciton to the collective modes of nanoplasmonic arrays. The absorption of the strongly coupled system exhibits polariton characteristics imprinted by the lattice, substantiating the system as a polaritonic metasurface with narrow-angle, directional and linearly polarized far-field emission profile. Replacing nanodiscs by chiral nanostructures would utilize the peculiar valleytronic properties of TMD monolayers for applications in opto-valleytronics.[56−58] Clearly, our fabrication method, that ensures both the integrity of TMD monolayer exciton resonances and their coupling to the near-field of the plasmonic SLRs, is not limited to square lattices. It can be straightforwardly adapted to other lattice geometries to provide a complementary approach to the engineering of collective effects in purely photonic lattices,[59] with a wide range of applications emulating exotic many-body phenomena such as Anderson localization[60] or topological insulators.[61]

https://doi.org/10.1021/acs.nanolett.4c02043
Nano Lett. 2024, 24, 10090−10097

METHODS

Sample Fabrication. The design of the gold nanodisk array with a lattice constant of 480 nm, disk diameters of 70 nm, and the height of 42 nm matching the hBN thickness was optimized in simulations with the finite-difference time-domain method (software Lumerical). The thickness of the second hBN layer was optimized for spectral resonance of the SRL and the bright exciton X in monolayer WSe_2. High-quality WSe_2 monolayers were synthesized by in-house chemical vapor deposition,[39] and hBN flakes were exfoliated from bulk crystals (NIMS). Gold nanodisk arrays embedded in hBN were fabricated by employing electron-beam lithography (EBL) and inductively coupled plasma (ICP) etching. A square array of nanodisks with a diameter of 70 nm was defined via EBL using PMMA 950 K resist with a thickness of 200 nm and a dose of 500 $\mu C/cm^2$. Through-holes were etched into the hBN via ICP. The plasma was generated by 5 sccm of Ar and 10 sccm of SF_6 at a constant chamber pressure of 10 mTorr. Setting the ICP power to 70 W and the RF power to 6 W yielded a controlled etch rate of 0.6 nm/s. After etching, a gold film matching the thickness of the hBN layer was deposited via electron-beam evaporation. The hardened resist was lifted-off in acetone and isopropanol, and remaining residues were removed in an O_2 asher.

For the assembly of the van der Waals metasurface, we used a dry stamping method with a polydimethylsiloxane (PDMS) droplet on a glass slide as stamp base, covered with a thin film of Poly(Bisphenol A-carbonate) (PC, Sigma-Aldrich) or polycaprolactone (PCL, Sigma-Aldrich). We created the PC (PCL) film by dispersing a solution of polymer dissolved in chloroform (tetrahydrofuran, THF) at a mass percentage of 8% (15%). A 4 nm bottom hBN flake was picked up with a PC stamp at 50 °C, released onto a glass substrate at 195 °C, and cleaned in chloroform, acetone, and isopropanol. For the pick-up of the hBN flake with the incorporated gold lattice, a PCL stamp was used. We started the process at 30 °C and heated up to 57 °C to cover the entire flake with the stamp. After cooling down to 30 °C, we lifted the flake with the embedded lattice off the substrate and released it onto a WSe_2 monolayer at 75 °C, followed by cleaning in THF, acetone, and isopropanol. Finally, a PC stamp was used to pick up the stack at 115 °C, followed by release onto the bottom hBN flake at 195 °C. The sample was cleaned in chloroform, acetone, and isopropanol and annealed in ultrahigh vacuum for 15 h at 200 °C to remove trapped air and residues.

The atomic force micrographs of the top and bottom sides of the hBN flake with incorporated gold lattice, shown in Figure 1b and c, were measured using the standard tapping mode height measurement. The top side was measured after the fabrication of the gold lattice, while the bottom side was measured while the flake was face down on the PDMS/PCL stamp before picking up the TMD monolayer.

Optical Spectroscopy. Cryogenic DR and PL spectroscopy were performed in backscattering geometry in a closed-cycle cryostat (attocube systems, attoDRY800) with a base temperature of 4 K. To position the sample with respect to a low temperature apochromatic objective (LT-APO/633-RAMAN/0.81), we used piezo-units (attocube systems, ANPx101, ANPz101, and ANSxy100). Angle-resolved DR and PL spectra were recorded with a lab-built Fourier imaging setup in 4f and telescope configuration employing four achromatic doublet lenses (Edmund Optics, VIS-NIR with focal lengths of 750, 750, 400, and 150 mm) and including a dove prism to rotate the Fourier image. The angle-resolved DR data of Figure 2 was acquired with linearly polarized excitation and detection (using linear polarizers in both excitation and detection pathways), while the angle-resolved PL of Figure 3a used linear polarized excitation but unpolarized detection (linear polarizer only in the excitation pathway). The signal was dispersed by a monochromator (Teledyne Princeton Instruments, IsoPlane SCT320), with a 300 grooves/mm grating and detected by a Peltier-cooled CCD (Teledyne Princeton Instruments, PIXIS 1024). Narrow-energy momentum-space images were recorded by turning two tunable filters (Semrock 790 nm VersaChrome Edge tunable Shortpass and Longpass Filters) at zero-order spectrometer grating and an open slit. The conversion of camera pixel to wavevector in $1/\mu m$ was obtained via the size of the illuminated area on the CCD and using the relation $k_{\parallel} = k_0 \sin(\Theta)$ with the maximum angle Θ given by the numerical aperture of the objective, and $k_0 = 2\pi/\lambda$. For both DR and PL measurements, we used a pulsed supercontinuum laser (NKT Photonics, SuperK with Varia). DR was defined as $DR = (R - R_0)/R_0$, where R was the reflactance from the sample and R_0 was the reference reflectance from a region containing only hBN. PL was excited at 662 ± 5 nm and 20 μW.

Plasmon-Exciton-Polariton Dispersion. The exciton-polariton dispersion was obtained from the coupled oscillator model[62] with the Hamiltonian:

$$H = \begin{pmatrix} E_X - i\gamma_X & g \\ g & E_{SLR} - i\gamma_{SLR} \end{pmatrix} \tag{3}$$

Diagonalization yields the well-known energy relation for the upper and lower polariton branches given by eq 2 in the main text. The Rabi splitting Ω, defined as[62]

$$\Omega = 2\sqrt{g^2 - \frac{1}{4}(\gamma_X - \gamma_{SLR})^2} \tag{4}$$

was determined experimentally as 44 ± 5 meV. The linewidth of the lower polariton branch is given by

$$\gamma_{LP} = |X|^2\gamma_X + |C|^2\gamma_{SLR} \tag{5}$$

where X and C are the Hopfield coefficients[63]

$$|X|^2 = \frac{1}{2}\left[1 + \frac{E_{SLR} - E_X}{\sqrt{\Omega^2 + (E_{SLR} - E_X)^2}}\right] \tag{6}$$

$$|C|^2 = \frac{1}{2}\left[1 - \frac{E_{SLR} - E_X}{\sqrt{\Omega^2 + (E_{SLR} - E_X)^2}}\right] \tag{7}$$

and shown as dashed cyan lines in Figures 2c and 3a for the hyperbolic polariton dispersion.

ASSOCIATED CONTENT

Data Availability Statement

The data that supports the findings of this study are available at https://data.ub.uni-muenchen.de/508/.

AUTHOR INFORMATION

Corresponding Authors

Farsane Tabataba-Vakili − *Fakultät für Physik, Munich Quantum Center, and Center for NanoScience (CeNS),*

https://doi.org/10.1021/acs.nanolett.4c02043
Nano Lett. 2024, 24, 10090−10097

Ludwig-Maximilians-Universität München, 80539 München, Germany; Munich Center for Quantum Science and Technology (MCQST), 80799 München, Germany; orcid.org/0000-0001-5911-7594; Email: f.tabataba@lmu.de

Alexander Högele − *Fakultät für Physik, Munich Quantum Center, and Center for NanoScience (CeNS), Ludwig-Maximilians-Universität München, 80539 München, Germany; Munich Center for Quantum Science and Technology (MCQST), 80799 München, Germany;* orcid.org/0000-0002-0178-9117; Email: alexander.hoegele@lmu.de

Authors

Lukas Krelle − *Fakultät für Physik, Munich Quantum Center, and Center for NanoScience (CeNS), Ludwig-Maximilians-Universität München, 80539 München, Germany;* Present Address: Institute for Condensed Matter Physics, Technische Universität Darmstadt, Hochschulstraße 6, 64289 Darmstadt, Germany

Lukas Husel − *Fakultät für Physik, Munich Quantum Center, and Center for NanoScience (CeNS), Ludwig-Maximilians-Universität München, 80539 München, Germany*

Huy P. G. Nguyen − *Fakultät für Physik, Munich Quantum Center, and Center for NanoScience (CeNS), Ludwig-Maximilians-Universität München, 80539 München, Germany*

Zhijie Li − *Fakultät für Physik, Munich Quantum Center, and Center for NanoScience (CeNS), Ludwig-Maximilians-Universität München, 80539 München, Germany*

Ismail Bilgin − *Fakultät für Physik, Munich Quantum Center, and Center for NanoScience (CeNS), Ludwig-Maximilians-Universität München, 80539 München, Germany*

Kenji Watanabe − *Research Center for Functional Materials, National Institute for Materials Science, Tsukuba 305-0044, Japan;* orcid.org/0000-0003-3701-8119

Takashi Taniguchi − *International Center for Materials Nanoarchitectonics, National Institute for Materials Science, Tsukuba 305-0044, Japan;* orcid.org/0000-0002-1467-3105

Complete contact information is available at: https://pubs.acs.org/10.1021/acs.nanolett.4c02043

Author Contributions

⊥F.T.-V. and L.K. contributed equally to this work.

Notes

The authors declare no competing financial interest.

■ ACKNOWLEDGMENTS

This research was funded by the European Research Council (ERC) under the Grant Agreement No. 772195 and the Deutsche Forschungsgemeinschaft (DFG, German Research Foundation) within Germany's Excellence Strategy under Grant No. EXC-2111-390814868. F.T.-V. acknowledges funding from the Munich Center for Quantum Science and Technology (MCQST) and the European Union's Framework Programme for Research and Innovation Horizon Europe under the Marie Skłodowska-Curie Actions Grant Agreement No. 101058981. K.W. and T.T. acknowledge support from the JSPS KAKENHI (Grant Nos. 20H00354 and 23H02052) and World Premier International Research Center Initiative (WPI), MEXT, Japan. A.H. acknowledges funding by the Bavarian Hightech Agenda within the EQAP project.

■ REFERENCES

(1) Yu, N.; Capasso, F. Flat optics with designer metasurfaces. *Nat. Mater.* **2014**, *13*, 139−150.
(2) Meinzer, N.; Barnes, W. L.; Hooper, I. R. Plasmonic meta-atoms and metasurfaces. *Nat. Photonics* **2014**, *8*, 889−898.
(3) Chen, H.-T.; Taylor, A. J.; Yu, N. A review of metasurfaces: physics and applications. *Rep. Prog. Phys.* **2016**, *79*, 076401.
(4) Yu, N.; Genevet, P.; Kats, M. A.; Aieta, F.; Tetienne, J.-P.; Capasso, F.; Gaburro, Z. Light propagation with phase discontinuities: generalized laws of reflection and refraction. *Science* **2011**, *334*, 333−337.
(5) Huang, L.; Chen, X.; Mühlenbernd, H.; Zhang, H.; Chen, S.; Bai, B.; Tan, Q.; Jin, G.; Cheah, K.-W.; Qiu, C.-W.; Li, J.; Zentgraf, T.; Zhang, S. Three-dimensional optical holography using a plasmonic metasurface. *Nat. Commun.* **2013**, *4*, 2808.
(6) Aieta, F.; Genevet, P.; Kats, M. A.; Yu, N.; Blanchard, R.; Gaburro, Z.; Capasso, F. Aberration-free ultrathin flat lenses and axicons at telecom wavelengths based on plasmonic metasurfaces. *Nano Lett.* **2012**, *12*, 4932−4936.
(7) Deng, S.; Li, R.; Park, J.-E.; Guan, J.; Choo, P.; Hu, J.; Smeets, P. J.; Odom, T. W. Ultranarrow plasmon resonances from annealed nanoparticle lattices. *Proc. Natl. Acad. Sci. U.S.A.* **2020**, *117*, 23380−23384.
(8) Cherqui, C.; Bourgeois, M. R.; Wang, D.; Schatz, G. C. Plasmonic surface lattice resonances: Theory and computation. *Acc. Chem. Res.* **2019**, *52*, 2548−2558.
(9) Guo, R.; Hakala, T. K.; Törmä, P. Geometry dependence of surface lattice resonances in plasmonic nanoparticle arrays. *Phys. Rev. B* **2017**, *95*, 155423.
(10) Meng, Y.; Zhong, H.; Xu, Z.; He, T.; Kim, J. S.; Han, S.; Kim, S.; Park, S.; Shen, Y.; Gong, M.; Xiao, Q.; Bae, S.-H. Functionalizing nanophotonic structures with 2D van der Waals materials. *Nanoscale Horiz.* **2023**, *8*, 1345−1365.
(11) Pizzocchero, F.; Gammelgaard, L.; Jessen, B. S.; Caridad, J. M.; Wang, L.; Hone, J.; Bøggild, P.; Booth, T. J. The hot pick-up technique for batch assembly of van der Waals heterostructures. *Nat. Commun.* **2016**, *7*, 11894.
(12) Splendiani, A.; Sun, L.; Zhang, Y.; Li, T.; Kim, J.; Chim, C.-Y.; Galli, G.; Wang, F. Emerging photoluminescence in monolayer MoS_2. *Nano Lett.* **2010**, *10*, 1271−1275.
(13) Mak, K. F.; Lee, C.; Hone, J.; Shan, J.; Heinz, T. F. Atomically thin MoS_2: a new direct-gap semiconductor. *Phys. Rev. Lett.* **2010**, *105*, 136805.
(14) He, K.; Kumar, N.; Zhao, L.; Wang, Z.; Mak, K. F.; Zhao, H.; Shan, J. Tightly bound excitons in monolayer WSe_2. *Phys. Rev. Lett.* **2014**, *113*, 026803.
(15) Chernikov, A.; Berkelbach, T. C.; Hill, H. M.; Rigosi, A.; Li, Y.; Aslan, B.; Reichman, D. R.; Hybertsen, M. S.; Heinz, T. F. Exciton binding energy and nonhydrogenic Rydberg series in monolayer WS_2. *Phys. Rev. Lett.* **2014**, *113*, 076802.
(16) Zhang, C.; Wang, H.; Chan, W.; Manolatou, C.; Rana, F. Absorption of light by excitons and trions in monolayers of metal dichalcogenide MoS_2: Experiments and theory. *Phys. Rev. B* **2014**, *89*, 205436.
(17) Li, Y.; Chernikov, A.; Zhang, X.; Rigosi, A.; Hill, H. M.; Van Der Zande, A. M.; Chenet, D. A.; Shih, E.-M.; Hone, J.; Heinz, T. F. Measurement of the optical dielectric function of monolayer transition-metal dichalcogenides: MoS_2, $MoSe_2$, WS_2, and WSe_2. *Phys. Rev. B* **2014**, *90*, 205422.
(18) Xiao, D.; Liu, G.-B.; Feng, W.; Xu, X.; Yao, W. Coupled spin and valley physics in monolayers of MoS_2 and other group-VI dichalcogenides. *Phys. Rev. Lett.* **2012**, *108*, 196802.
(19) Mak, K. F.; He, K.; Shan, J.; Heinz, T. F. Control of valley polarization in monolayer MoS_2 by optical helicity. *Nat. Nanotechnol.* **2012**, *7*, 494−498.

(20) Wang, G.; Chernikov, A.; Glazov, M. M.; Heinz, T. F.; Marie, X.; Amand, T.; Urbaszek, B. Colloquium: Excitons in atomically thin transition metal dichalcogenides. *Rev. Mod. Phys.* **2018**, *90*, 021001.
(21) Van de Groep, J.; Song, J.-H.; Celano, U.; Li, Q.; Kik, P. G.; Brongersma, M. L. Exciton resonance tuning of an atomically thin lens. *Nat. Photonics* **2020**, *14*, 426−430.
(22) Sun, L.; Wang, C.-Y.; Krasnok, A.; Choi, J.; Shi, J.; Gomez-Diaz, J. S.; Zepeda, A.; Gwo, S.; Shih, C.-K.; Alù, A.; Li, X. Separation of valley excitons in a MoS_2 monolayer using a subwavelength asymmetric groove array. *Nat. Photonics* **2019**, *13*, 180−184.
(23) Dufferwiel, S.; Schwarz, S.; Withers, F.; Trichet, A.; Li, F.; Sich, M.; Del Pozo-Zamudio, O.; Clark, C.; Nalitov, A.; Solnyshkov, D.; Malpuech, G.; Novoselov, K. S.; Smith, J. M.; Skolnick, M. S.; Krizhanovskii, D. N.; Tartakovskii, A. I. Exciton−polaritons in van der Waals heterostructures embedded in tunable microcavities. *Nat. Commun.* **2015**, *6*, 8579.
(24) Liu, X.; Galfsky, T.; Sun, Z.; Xia, F.; Lin, E.-c.; Lee, Y.-H.; Kéna-Cohen, S.; Menon, V. M. Strong light−matter coupling in two-dimensional atomic crystals. *Nat. Photonics* **2015**, *9*, 30−34.
(25) Chen, Y.; Miao, S.; Wang, T.; Zhong, D.; Saxena, A.; Chow, C.; Whitehead, J.; Gerace, D.; Xu, X.; Shi, S.-F.; Majumdar, A. Metasurface integrated monolayer exciton polariton. *Nano Lett.* **2020**, *20*, 5292−5300.
(26) Liu, W.; Lee, B.; Naylor, C. H.; Ee, H.-S.; Park, J.; Johnson, A. C.; Agarwal, R. Strong exciton−plasmon coupling in MoS_2 coupled with plasmonic lattice. *Nano Lett.* **2016**, *16*, 1262−1269.
(27) Wang, S.; Le-Van, Q.; Vaianella, F.; Maes, B.; Eizagirre Barker, S.; Godiksen, R. H.; Curto, A. G.; Gomez Rivas, J. Limits to strong coupling of excitons in multilayer WS_2 with collective plasmonic resonances. *ACS Photonics* **2019**, *6*, 286−293.
(28) Liu, W.; Wang, Y.; Zheng, B.; Hwang, M.; Ji, Z.; Liu, G.; Li, Z.; Sorger, V. J.; Pan, A.; Agarwal, R. Observation and active control of a collective polariton mode and polaritonic band gap in few-layer WS_2 strongly coupled with plasmonic lattices. *Nano Lett.* **2020**, *20*, 790−798.
(29) Khatibi, Z.; Feierabend, M.; Selig, M.; Brem, S.; Linderälv, C.; Erhart, P.; Malic, E. Impact of strain on the excitonic linewidth in transition metal dichalcogenides. *2D Mater.* **2019**, *6*, 015015.
(30) Raja, A.; Waldecker, L.; Zipfel, J.; Cho, Y.; Brem, S.; Ziegler, J. D.; Kulig, M.; Taniguchi, T.; Watanabe, K.; Malic, E.; Heinz, T. F.; Berkelbach, T. C.; Chernikov, A. Dielectric disorder in two-dimensional materials. *Nat. Nanotechnol.* **2019**, *14*, 832−837.
(31) Cadiz, F.; Courtade, E.; Robert, C.; Wang, G.; Shen, Y.; Cai, H.; Taniguchi, T.; Watanabe, K.; Carrere, H.; Lagarde, D.; Manca, M.; Amand, T.; Renucci, P.; Tongay, S.; Marie, X.; Urbaszek, B. Excitonic linewidth approaching the homogeneous limit in MoS_2-based van der Waals heterostructures. *Phys. Rev. X* **2017**, *7*, 021026.
(32) Wang, S.; Li, S.; Chervy, T.; Shalabney, A.; Azzini, S.; Orgiu, E.; Hutchison, J. A.; Genet, C.; Samorì, P.; Ebbesen, T. W. Coherent coupling of WS_2 monolayers with metallic photonic nanostructures at room temperature. *Nano Lett.* **2016**, *16*, 4368−4374.
(33) Sun, J.; Li, Y.; Hu, H.; Chen, W.; Zheng, D.; Zhang, S.; Xu, H. Strong plasmon−exciton coupling in transition metal dichalcogenides and plasmonic nanostructures. *Nanoscale* **2021**, *13*, 4408−4419.
(34) Su, G.; Gao, A.; Peng, B.; Hu, J.; Zhang, Y.; Liu, F.; Zhang, H.; Zhan, P.; Wu, W. Observation of in-plane exciton−polaritons in monolayer WSe_2 driven by plasmonic nanofingers. *Nanophotonics* **2022**, *11*, 3149−3157.
(35) Guo, C.; Yu, J.; Deng, S. Hybrid metasurfaces of plasmonic lattices and 2D materials. *Adv. Funct. Mater.* **2023**, *33*, 2302265.
(36) Klein, M.; Badada, B. H.; Binder, R.; Alfrey, A.; McKie, M.; Koehler, M. R.; Mandrus, D. G.; Taniguchi, T.; Watanabe, K.; LeRoy, B. J.; Schaibley, J. R. 2D semiconductor nonlinear plasmonic modulators. *Nat. Commun.* **2019**, *10*, 3264.
(37) Dibos, A. M.; Zhou, Y.; Jauregui, L. A.; Scuri, G.; Wild, D. S.; High, A. A.; Taniguchi, T.; Watanabe, K.; Lukin, M. D.; Kim, P.; Park, H. Electrically tunable exciton−plasmon coupling in a WSe_2 monolayer embedded in a plasmonic crystal cavity. *Nano Lett.* **2019**, *19*, 3543−3547.
(38) Vadia, S.; Scherzer, J.; Watanabe, K.; Taniguchi, T.; Högele, A. Magneto-optical chirality in a coherently coupled exciton−plasmon system. *Nano Lett.* **2023**, *23*, 614−618.
(39) Li, Z.; Förste, J.; Watanabe, K.; Taniguchi, T.; Urbaszek, B.; Baimuratov, A. S.; Gerber, I. C.; Högele, A.; Bilgin, I. Stacking-dependent exciton multiplicity in WSe_2 bilayers. *Phys. Rev. B* **2022**, *106*, 045411.
(40) Baranov, D. G.; Wersall, M.; Cuadra, J.; Antosiewicz, T. J.; Shegai, T. Novel nanostructures and materials for strong light−matter interactions. *ACS Photonics* **2018**, *5*, 24−42.
(41) Schneider, C.; Glazov, M. M.; Korn, T.; Höfling, S.; Urbaszek, B. Two-dimensional semiconductors in the regime of strong light-matter coupling. *Nat. Commun.* **2018**, *9*, 2695.
(42) You, Y.; Zhang, X.-X.; Berkelbach, T. C.; Hybertsen, M. S.; Reichman, D. R.; Heinz, T. F. Observation of biexcitons in monolayer WSe_2. *Nat. Phys.* **2015**, *11*, 477−481.
(43) Barbone, M.; Montblanch, A. R.-P.; Kara, D. M.; Palacios-Berraquero, C.; Cadore, A. R.; De Fazio, D.; Pingault, B.; Mostaani, E.; Li, H.; Chen, B.; Watanabe, K.; Taniguchi, T.; Tongay, S.; amd Andrea C. Ferrari, G. W.; Atatüre, M. Charge-tuneable biexciton complexes in monolayer WSe_2. *Nat. Commun.* **2018**, *9*, 3721.
(44) Li, Z.; Wang, T.; Lu, Z.; Jin, C.; Chen, Y.; Meng, Y.; Lian, Z.; Taniguchi, T.; Watanabe, K.; Zhang, S.; Smirnov, D.; Shi, S.-F. Revealing the biexciton and trion-exciton complexes in BN encapsulated WSe_2. *Nat. Commun.* **2018**, *9*, 3719.
(45) Steinhoff, A.; Florian, M.; Singh, A.; Tran, K.; Kolarczik, M.; Helmrich, S.; Achtstein, A. W.; Woggon, U.; Owschimikow, N.; Jahnke, F.; Li, X. Biexciton fine structure in monolayer transition metal dichalcogenides. *Nat. Phys.* **2018**, *14*, 1199−1204.
(46) Zhang, X.-X.; You, Y.; Zhao, S. Y. F.; Heinz, T. F. Experimental evidence for dark excitons in monolayer WSe_2. *Phys. Rev. Lett.* **2015**, *115*, 257403.
(47) Robert, C.; Amand, T.; Cadiz, F.; Lagarde, D.; Courtade, E.; Manca, M.; Taniguchi, T.; Watanabe, K.; Urbaszek, B.; Marie, X. Fine structure and lifetime of dark excitons in transition metal dichalcogenide monolayers. *Phys. Rev. B* **2017**, *96*, 155423.
(48) Courtade, E.; Semina, M.; Manca, M.; Glazov, M.; Robert, C.; Cadiz, F.; Wang, G.; Taniguchi, T.; Watanabe, K.; Pierre, M.; Escoffier, W.; Ivchenko, E. L.; Renucci, P.; Marie, X.; Amand, T.; Urbaszek, B. Charged excitons in monolayer WSe_2: Experiment and theory. *Phys. Rev. B* **2017**, *96*, 085302.
(49) He, M.; Rivera, P.; Van Tuan, D.; Wilson, N. P.; Yang, M.; Taniguchi, T.; Watanabe, K.; Yan, J.; Mandrus, D. G.; Yu, H.; Dery, H.; Yao, W.; Xu, X. Valley phonons and exciton complexes in a monolayer semiconductor. *Nat. Commun.* **2020**, *11*, 618.
(50) Liu, E.; van Baren, J.; Liang, C.-T.; Taniguchi, T.; Watanabe, K.; Gabor, N. M.; Chang, Y.-C.; Lui, C. H. Multipath optical recombination of intervalley dark excitons and trions in monolayer WSe_2. *Phys. Rev. Lett.* **2020**, *124*, 196802.
(51) Yang, M.; Ren, L.; Robert, C.; Van Tuan, D.; Lombez, L.; Urbaszek, B.; Marie, X.; Dery, H. Relaxation and darkening of excitonic complexes in electrostatically doped monolayer WSe_2: Roles of exciton-electron and trion-electron interactions. *Phys. Rev. B* **2022**, *105*, 085302.
(52) Förste, J.; Tepliakov, N. V.; Kruchinin, S. Y.; Lindlau, J.; Funk, V.; Förg, M.; Watanabe, K.; Taniguchi, T.; Baimuratov, A. S.; Högele, A. Exciton g-factors in monolayer and bilayer WSe_2 from experiment and theory. *Nat. Commun.* **2020**, *11*, 4539.
(53) Zeng, H.; Dai, J.; Yao, W.; Xiao, D.; Cui, X. Valley polarization in MoS_2 monolayers by optical pumping. *Nat. Nanotechnol.* **2012**, *7*, 490−493.
(54) Jones, A. M.; Yu, H.; Ghimire, N. J.; Wu, S.; Aivazian, G.; Ross, J. S.; Zhao, B.; Yan, J.; Mandrus, D. G.; Xiao, D.; Yao, W.; Xu, X. Optical generation of excitonic valley coherence in monolayer WSe_2. *Nat. Nanotechnol.* **2013**, *8*, 634−638.
(55) Wang, G.; Marie, X.; Liu, B.; Amand, T.; Robert, C.; Cadiz, F.; Renucci, P.; Urbaszek, B. Control of exciton valley coherence in transition metal dichalcogenide monolayers. *Phys. Rev. Lett.* **2016**, *117*, 187401.

https://doi.org/10.1021/acs.nanolett.4c02043
Nano Lett. 2024, 24, 10090−10097

(56) Gong, S.-H.; Alpeggiani, F.; Sciacca, B.; Garnett, E. C.; Kuipers, L. Nanoscale chiral valley-photon interface through optical spin-orbit coupling. *Science* **2018**, *359*, 443−447.
(57) Hu, G.; Hong, X.; Wang, K.; Wu, J.; Xu, H.-X.; Zhao, W.; Liu, W.; Zhang, S.; Garcia-Vidal, F.; Wang, B.; Lu, P.; Qiu, C.-W. Coherent steering of nonlinear chiral valley photons with a synthetic Au-WS_2 metasurface. *Nat. Photonics* **2019**, *13*, 467−472.
(58) Guddala, S.; Bushati, R.; Li, M.; Khanikaev, A.; Menon, V. Valley selective optical control of excitons in 2D semiconductors using a chiral metasurface. *Opt. Mater. Express* **2019**, *9*, 536−543.
(59) Ozawa, T.; Price, H. M.; Amo, A.; Goldman, N.; Hafezi, M.; Lu, L.; Rechtsman, M. C.; Schuster, D.; Simon, J.; Zilberberg, O.; Carusotto, I. Topological photonics. *Rev. Mod. Phys.* **2019**, *91*, 015006.
(60) Schwartz, T.; Bartal, G.; Fishman, S.; Segev, M. Transport and Anderson localization in disordered two-dimensional photonic lattices. *Nature* **2007**, *446*, 52−55.
(61) Rechtsman, M. C.; Zeuner, J. M.; Plotnik, Y.; Lumer, Y.; Podolsky, D.; Dreisow, F.; Nolte, S.; Segev, M.; Szameit, A. Photonic Floquet topological insulators. *Nature* **2013**, *496*, 196−200.
(62) Savona, V.; Andreani, L.; Schwendimann, P.; Quattropani, A. Quantum well excitons in semiconductor microcavities: Unified treatment of weak and strong coupling regimes. *Solid State Commun.* **1995**, *93*, 733−739.
(63) Hopfield, J. Theory of the contribution of excitons to the complex dielectric constant of crystals. *Phys. Rev.* **1958**, *112*, 1555.

https://doi.org/10.1021/acs.nanolett.4c02043
Nano Lett. 2024, 24, 10090−10097